PHYSICAL REVIEW B **89**, 045110 (2014)

Plasmon losses in core-level photoemission spectra studied by the quantum Landau formula including full multiple scattering

Misato Kazama, Hiroshi Shinotsuka, Yusuke Ohori, Kaori Niki,[*] and Takashi Fujikawa
Graduate School of Advanced Integration Science, Chiba University, 1-33 Yayoi-cho, Inage, Chiba 263-8522, Japan

László Kövér
Institute of Nuclear Research, HAS, PO Box 51, H-4001 Debrecen, Hungary

(Received 1 May 2013; revised manuscript received 28 October 2013; published 9 January 2014)

We study the angular and energy dependence of surface and bulk plasmon losses accompanying deep core excitations in simple metals. Here full multiple scatterings of photoelectrons are taken into account before and after the plasmon losses within the quantum Landau formula, which can describe overall features of the photoemission bands. For example, multiple plasmon loss features can be calculated by use of the formula. Two simple metals, Al and Na, are studied here. The depth profiles of the plasmon losses are strongly influenced by the elastic scatterings. The model assuming single elastic scatterings overestimates the losses from deep emitters due to the forward focusing effects, whereas the model accounting for full multiple scatterings gives a much rapidly decaying function of the depth due to the defocusing effects and rich structures due to the photoelectron diffraction. The single elastic scattering approximation gives a poor result both for the depth profiles and for the loss spectra. The present multiple scattering calculations successfully explain the azimuthal dependence of the loss spectra, which reflect the local geometry around the emitters.

DOI: 10.1103/PhysRevB.89.045110 PACS number(s): 78.68.+m, 71.45.Gm, 79.60.−i

I. INTRODUCTION

X-ray photoelectron spectroscopy (XPS) is now widely used for studying physical properties of materials. Plasmon satellites are observed in higher binding energy region than the main peaks in XPS spectra of simple metals and some semiconductors, notably Na, Al, Mg, and Si, Ge. The plasmon excitation mechanism has been in the focus of the photoemission studies since their early days of the photoemission study. The energy loss by the plasmon excitation can occur due to sudden creation of the core-hole potential (*intrinsic* process) or inelastic scattering during the transport of photoelectrons toward the solid surface (*extrinsic* process). These two excitation processes cannot be distinguished in principle: They can interfere with each other, which is discussed from theoretical sides[1–5] and experimental sides.[6,7]

For the practical calculations, semiclassical approaches are often employed, where the photoelectron propagations inside the solids are described by a classical trajectory.[8–11] Sophisticated many-body one-step quantum theories have been developed on the basis of many-body scattering theory by use of projection operator techniques.[4,5] On the other hand first principle formal photoemission theories based on Keldysh Green's functions were at first proposed by Caroli *et al.*[12] and further refined by Almbladh.[13] A practical method has been developed to calculate x-ray photoelectron diffraction (XPD) spectra based on the Keldysh Green's function approach.[14,15] Great advantages of this theoretical framework are feasibility of radiation field effects[16–18] and relativistic effects.[19] In this study, however, we discuss the plasmon losses within the nonrelativistic theory. Both the many-body scattering theory and the Keldysh Green's function theory provide us with very similar formulas: We apply the latter approach to the present work.

Starting from a first principle many-body theory, Hedin *et al.* have derived a quantum Landau formula, which describes overall features in core-level photoemission spectra including plasmon satellite peaks and asymmetry of main peaks due to x-ray singularity.[5] We should note that the quantum Landau formula works well in the high-energy region. Ohori *et al.* have investigated the applicability of the quantum Landau formula for the plasmon losses without elastic scatterings.[20] Their results show that the Quantum Landau formula gives results quite similar to those without use of the high-energy approximation in the photoelectron kinetic energy range from 60 to 1000 eV. Uwatoko *et al.* have measured and calculated single plasmon loss spectra associated with Al $2p$ photoemission on the basis of Hedin's formalism,[6] which shows rather good results as far as we include the interference. In Hedin's approach, elastic scatterings inside the solids are completely neglected. It has been reported, however, that plasmon peaks are strongly influenced by the photoelectron diffraction,[21] and it is thus important to consider the elastic scatterings to analyze the experimental results in detail. A new quantum Landau formula has been derived by Fujikawa *et al.*, where the elastic scatterings before and after the loss are fully taken into account.[22] This formula is a powerful tool to study the plasmon losses including higher order satellites. So far Kazama *et al.* have applied that theoretical approach to the plasmon losses associated with Al $2s$ photoemission. The single scattering model gives rise to unexpected large loss intensities from deep emitters and the overestimated strong bulk plasmon loss intensity.[23]

In this paper we study plasmon satellite peaks in XPS spectra based on the new quantum Landau formula taking full multiple scatterings into account. In Sec. II we discuss the theoretical framework to obtain the quantum Landau formula, and then in Sec. III we show some calculated results taking full multiple scatterings into account. These results are compared

©2014 American Physical Society

with those without elastic scatterings or with only single scatterings to study the photoelectron diffraction effects on plasmon loss features.

II. THEORY

In this section we discuss the basic formulas used in the present theoretical analyses.

A. No-loss and single-loss intensities

The intensity measuring photoelectrons with momentum $\mathbf{p}$ and kinetic energy $\varepsilon_p = p^2/2$ at the main XPS band (no loss band) excited by x-ray photons with the energy ω is described in terms of the damped photoelectron wave function $f_{\mathbf{p}}^-$ under the influence of the optical potential for the excitation from the core level c,[4,14]

$$I(\boldsymbol{p};\omega)^0 = 2\pi|\langle f_{\boldsymbol{p}}^-|\Delta|\phi_c\rangle S_0|^2\delta(E_0+\omega-E_0^*-\varepsilon_p), \tag{1}$$

where ϕ_c is the core wave function localized on the site A. Ground state energies with and without a core hole are represented by E_0^* and E_0, and Δ is the electron-photon interaction operator. The intrinsic no-loss amplitude S_0 should be close to 1. The amplitude $\langle f_{\boldsymbol{p}}^-|\Delta|\phi_c\rangle$ can be calculated by using full multiple-scattering formula as used in photoelectron diffraction calculations.[24–27]

The single-loss XPS intensity, whose loss energy is ω_m, is written as[14]

$$\begin{aligned} I(\boldsymbol{p};\omega)^1 = 2\pi\sum_m &|\langle f_{\boldsymbol{p}}^-|\Delta|\phi_c\rangle S_m \\ &+\langle f_{\boldsymbol{p}}^-|v_m g(\varepsilon_p+\omega_m)\Delta|\phi_c\rangle S_0|^2 \\ &\times\delta(E_0+\omega-E_0^*-\omega_m-\varepsilon_p). \end{aligned} \tag{2}$$

v_m is the fluctuation potential associated with the excitation $0^*\to m^*$, which is responsible for the intrinsic and the extrinsic excitations, and $g(\varepsilon_p+\omega_m)$ is the causal Green's function. The first and second terms in $|\cdots|^2$ describe the intrinsic and extrinsic loss processes. Intrinsic amplitudes S_0, $S_n(n>0)$ are defined by

$$S_0 = \langle 0^*|b|0\rangle, \tag{3}$$

$$S_n = \langle n^*|b|0\rangle, \tag{4}$$

where b is the annihilation operator associated with the core state ϕ_c. A well-known Hamiltonian is introduced to obtain more information for the practical calculations:[28]

$$H = H_v + \varepsilon_c b^\dagger b + V_c b b^\dagger. \tag{5}$$

In Eq. (5) H_v is the full many-electron Hamiltonian for valence electrons, V_c is an interaction between the core-hole and valence electrons, and ε_c is a core electron energy. A hole state $|n_v^*\rangle$ satisfies

$$H^*|n_v^*\rangle = E_n^*|n_v^*\rangle, \tag{6}$$

where $H^* = H_v + V_c$. The ground state of the no hole Hamiltonian $H_v+\varepsilon_c$ is $|0\rangle = |0_v\rangle|c\rangle$. The intrinsic amplitudes are simplified by using this approximate Hamiltonian and conventional perturbation theory as

$$\begin{aligned} &S_0 = \exp(-a/2), \\ &S_n = -\frac{\langle c|v_n|c\rangle}{\omega_n}\exp(-a/2), \quad \omega_n = E_n^*-E_0^*. \end{aligned} \tag{7}$$

The fluctuation potential associated with the excitation $0_v^*\to n_v^*$ is defined by use of the bare Coulomb potential $v(\mathbf{r}-\mathbf{r}')$

$$v_n(\boldsymbol{r}) = \int d\boldsymbol{r}'v(\boldsymbol{r}-\boldsymbol{r}')\langle n_v^*|\psi^\dagger(\boldsymbol{r}')\psi(\boldsymbol{r}')|0_v^*\rangle. \tag{8}$$

The renormalization factor a is given by

$$a = \sum_{n>0}\frac{|\langle c|v_n|c\rangle|^2}{\omega_n^2}. \tag{9}$$

We apply the site T-matrix expansion for $f_{\mathbf{p}}^-$ and $g(\varepsilon_p+\omega_m)$ to calculate the extrinsic loss term in Eq. (2):[22]

$$\begin{aligned} &\langle f_{\boldsymbol{p}}^-|v_m g(\varepsilon_p+\omega_m)\Delta|\phi_c\rangle \\ &\quad= \langle\phi_{\boldsymbol{p}}^0|\left(1+\sum_\alpha t_\alpha g_0+\sum_{\alpha\neq\alpha'}t_{\alpha'}g_0t_\alpha g_0+\cdots\right)v_m \\ &\qquad\times\left(g_A'+\sum_\beta g_0't_\beta'g_A'+\cdots\right)\Delta|\phi_c\rangle. \end{aligned} \tag{10}$$

Here an abbreviation $g_A' = g_A(\varepsilon_p+\omega_m)$ is used. The damping plane wave $\phi_{\boldsymbol{p}}^0$ has the complex momentum $p_z = \tilde{p}$ and the real parallel components $\boldsymbol{p}_\parallel = (p_x,p_y)$, $\mathbf{r}_\parallel = (x,y)$:

$$\phi_{\boldsymbol{p}}^0 = \exp(i\boldsymbol{p}_\parallel\cdot\boldsymbol{r}_\parallel)\exp(i\tilde{p}z). \tag{11}$$

The fluctuation potential v_m defined by Eq. (8) can be specified by a wave vector $\boldsymbol{q} = (q_x,q_y,0)$ with the aid of translational symmetry parallel to the surface:

$$v_m(\boldsymbol{r}) = \exp(i\boldsymbol{q}\cdot\boldsymbol{r}_\parallel)V_m(z), \quad \boldsymbol{r} = (\boldsymbol{r}_\parallel,z). \tag{12}$$

We assume that the solid occupies the region $z\leqslant 0$. Then the z component of $\boldsymbol{p}$ should be written by use of the imaginary part of the optical potential Γ:

$$\tilde{p} = \sqrt{p_z^2-2i\Gamma}. \tag{13}$$

The lowest order extrinsic loss amplitude

$$\tau_{\rm ex}^{(0)}(\boldsymbol{p}) = \langle\phi_{\boldsymbol{p}}^0|v_m g_A'\Delta|\phi_c\rangle \tag{14}$$

neglects whole elastic scatterings from surrounding atoms before and after the loss. The propagator $g_A'(\boldsymbol{r},\boldsymbol{r}')$ in the amplitude $\tau_{\rm ex}^{(0)}$ is given in angular momentum representation,

$$g_A'(\boldsymbol{r},\boldsymbol{r}') = -2ip'\sum_L h_l(p'r_>)Y_L(\hat{\boldsymbol{r}})R_l^A(p'r_<)Y_L^*(\hat{\boldsymbol{r}}')\exp\left(i\delta_l^A\right), \tag{15}$$

where $\mathbf{p}'(\parallel\mathbf{p})$ is the momentum of the photoelectrons before the loss and R_l^A is the regular radial solution for the spherically symmetric potential v_A at the x-ray absorbing atom A. As the core function ϕ_c is strongly localized on the atomic site A, it can be safely assumed that the condition $r>r'$ is always satisfied. It is convenient to use the integral representation

$$-2ip'h_l(p'r)Y_L(\hat{\boldsymbol{r}}) = \frac{i^{-l}}{\pi^2}\int d\boldsymbol{k}Y_L(\hat{\boldsymbol{k}})\frac{\exp(i\boldsymbol{k}\cdot\boldsymbol{r})}{p'^2 - k^2 + 2i\Gamma}, \quad (16)$$

and thus

$$\tau_{\rm ex}^{(0)} = \sum_L \frac{i^{-l}}{\pi^2}\int \frac{Y_L(\hat{\boldsymbol{k}})}{p'^2 - k^2 + 2i\Gamma}\langle\phi_{\boldsymbol{p}}^0|v_m|e^{i\boldsymbol{k}\cdot(\boldsymbol{r}-\boldsymbol{R}_A)}\rangle d\boldsymbol{k}M'_{LL_c}, \quad (17)$$

where M'_{LL_c} is an atomic excitation matrix element with the energy of $\varepsilon_p + \omega_m$,

$$M'_{LL_c}(\boldsymbol{p}) = \exp\left(i\delta_l^A\right)\rho(l)_c G(L_c 10|L). \quad (18)$$

The Gaunt integral $G(L_c 10|L)$ is responsible for the dipole excitation selection rule, $\rho(l)_c$ is the radial dipole matrix element between the core function and lth partial photoelectron wave. Now we evaluate the amplitude $\langle\phi_{\boldsymbol{p}}^0|v_m|e^{i\boldsymbol{k}\cdot(\boldsymbol{r}-\boldsymbol{R}_A)}\rangle$ with the aid of formula (12) for v_m:[22]

$$\begin{aligned}\tau_{\rm ex}^0(\boldsymbol{p}) &= \sum_L \frac{i^{-l}}{\pi^2}(2\pi)^{1/2}e^{-i\tilde{p}^* z_A}\int dk_z\frac{Y_L(\hat{\boldsymbol{k}}')}{\kappa^2 - k_z^2 + 2i\Gamma}\\ &\quad\times\int_{-\infty}^{\infty} V_m(z)e^{i(k_z-\tilde{p}^*)(z-z_A)}dz M'_{LL_c},\\ \boldsymbol{k}' &= (\boldsymbol{p}_\parallel - \boldsymbol{q}, k_z),\\ \kappa &= \sqrt{p'^2 - (\boldsymbol{p}_\parallel - \boldsymbol{q})^2} = \sqrt{p^2 + 2\omega_m - (\boldsymbol{p}_\parallel - \boldsymbol{q})^2}.\end{aligned} \quad (19)$$

The main contribution to the integral over k_z in Eq. (19) comes from the very small region near $k_z \sim \kappa$ because of the factor $(\kappa^2 - k_z^2 + 2i\Gamma)^{-1}$. The spherical harmonics $Y_L(\hat{\boldsymbol{k}}')$ changes very slowly with k_z and $Y_L(\hat{\boldsymbol{k}}')$ can be replaced by $Y_L(\hat{\boldsymbol{Q}}')$, where

$$\boldsymbol{Q}' = (\boldsymbol{p}_\parallel - \boldsymbol{q}, \kappa). \quad (20)$$

Then the integral over k_z is calculated as

$$\int dk_z\frac{\exp[ik_z(z - z_A)]}{k_z^2 - \kappa^2 + 2i\Gamma} = \frac{\pi i}{\tilde{\kappa}}e^{i\kappa|z-z_A|}, \quad \tilde{\kappa} = \sqrt{\kappa^2 + 2i\Gamma}. \quad (21)$$

Substituting Eq. (21) into Eq. (19), we obtain the extrinsic loss amplitude:

$$\tau_{\rm ex}^{(0)}(\boldsymbol{p}) \approx -g_{\rm ex}^m(A;\boldsymbol{p})\exp(-i\tilde{p}^* z_A)\sqrt{\frac{2}{\pi}}\sum_L i^{-l}Y_L(\hat{\boldsymbol{Q}}')M'_{LL_c}. \quad (22)$$

The extrinsic loss amplitude $g_{\rm ex}^m$ in the above formula is given in terms of the fluctuation potential V_m:

$$\begin{aligned}g_{\rm ex}^m(A;\boldsymbol{p}) &= \frac{i}{\tilde{\kappa}}\left[\int_{-\infty}^{z_A} dz V_m(z)e^{-i(\tilde{\kappa}+\tilde{p}^*)(z-z_A)}\right.\\ &\quad\left.+\int_{z_A}^{\infty} dz V_m(z)e^{i(\tilde{\kappa}-\tilde{p}^*)(z-z_A)}\right],\\ \tilde{\kappa} &= \sqrt{\kappa^2 + 2i\Gamma}.\end{aligned} \quad (23)$$

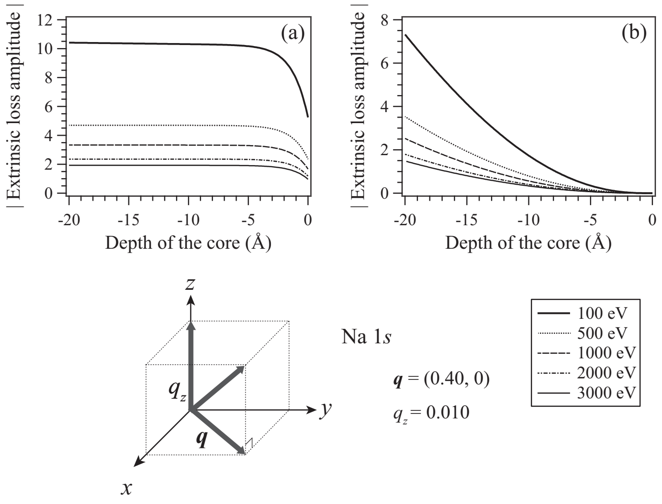

FIG. 1. Calculated $|g_{\rm ex}^m|$ for (a) surface and (b) bulk plasmon losses excited from Na 1s core level for different photoelectron kinetic energies from 100 to 3000 eV. Take-off angle is 90° (normal emission).

In the same way, a practical formula, which includes single-elastic scatterings before the loss, is obtained as follows:[22]

$$\begin{aligned}\tau_{\rm ex}^{(1)}(\boldsymbol{p}) &= \sum_\beta\langle\phi_{\boldsymbol{p}}^0|v_m g'_0 t'_\beta g'_A\Delta|\phi_c\rangle\\ &= -\sum_\beta g_{\rm ex}^m(\beta;\boldsymbol{p})e^{-i(\tilde{p}^* z_\beta + \boldsymbol{p}_\parallel\cdot\boldsymbol{R}_{\beta\parallel})}\\ &\quad\times\sqrt{\frac{2}{\pi}}\sum_{LL'} i^{-l'}Y_{L'}(\hat{\boldsymbol{Q}}')t_{l'}^\beta(p')G_{L'L}(p'\boldsymbol{R}_\beta)M'_{LL_c}.\end{aligned} \quad (24)$$

In the high-energy case, we expect that the site dependence of $g_{\rm ex}^m(\beta;\boldsymbol{p})$ can be neglected. Figures 1(a) and 1(b) show the depth dependence of the magnitude of the extrinsic loss amplitude $|g_{\rm ex}^m(\beta;\boldsymbol{p})|$ for the different photon energies from 100 to 3000 eV excited from Na. The surface (a) and bulk (b) plasmon losses are separately considered, where the hydrodynamic fluctuation potential by Inglesfield is used.[1] Both of them show slowly varying functions of the depth of the emitter. Then $g_{\rm ex}^m(\beta;\boldsymbol{p})$ can be replaced with $g_{\rm ex}^m(A;\boldsymbol{p})$ in Eq. (24). Furthermore except for nearly parallel photoemission to the surface plane, we can safely put $\hat{\boldsymbol{Q}}' \approx \hat{\boldsymbol{p}}$ in the high-energy region. The renormalization of the multiple scattering series before the loss is thus written with the aid of these two approximations:

$$\begin{aligned}&\tau_{\rm ex}^{(0)}(\boldsymbol{p}) + \tau_{\rm ex}^{(1)}(\boldsymbol{p}) + \cdots\\ &\quad= -g_{\rm ex}^m(A;\boldsymbol{p})\sum_\beta e^{-i(\tilde{p}^* z_\beta + \boldsymbol{p}_\parallel\cdot\boldsymbol{R}_{\beta\parallel})}\\ &\qquad\times\sqrt{\frac{2}{\pi}}\sum_{LL'\beta} i^{-l'}Y_{L'}(\hat{\boldsymbol{p}})[(1-X)^{-1}]_{L'L}^{\beta A}M'_{LL_c}\\ &\quad= -g_{\rm ex}^m(A;\boldsymbol{p})\langle f_{\boldsymbol{p}'}^-|\Delta|\phi_c\rangle,\end{aligned} \quad (25)$$

where X has been used in XPD and XANES analyses and $(1-X)^{-1}$ describes the renormalized full multiple scatterings.[24]

The loss amplitude $g_{\rm ex}^m$ defined by Eq. (23) can be rewritten in an alternative form in terms of the damping propagator g_0 defined by $g_0(\varepsilon)=(\varepsilon-T_e+i\Gamma)^{-1}$:

$$g_{\rm ex}^m(A;\boldsymbol{p})=-(2\pi)^{3/2}\int d\boldsymbol{r}\phi_{\boldsymbol{p}}^{0*}(\boldsymbol{r})v_m(\boldsymbol{r})g_0(\boldsymbol{r}-\boldsymbol{R}_A;p'). \tag{26}$$

We have so far taken the full multiple scatterings into account before the loss. Elastic scatterings after the loss can be fully taken into account in the same way:

$$\tau_{\rm ex}(\boldsymbol{p})\approx(2\pi)^{3/2}\langle f_{\boldsymbol{p}'}^-|\Delta|\phi_c\rangle\int d\boldsymbol{r}f_{\boldsymbol{p}}^{-*}(\boldsymbol{r})v_m(\boldsymbol{r})g_0(\boldsymbol{r}-\boldsymbol{R}_A;p'). \tag{27}$$

In the high-energy photoemission, $\langle f_{\boldsymbol{p}'}^-|\Delta|\phi_c\rangle$ can be safely replaced with $\langle f_{\boldsymbol{p}}^-|\Delta|\phi_c\rangle$, which yields an approximate extrinsic loss amplitude [the second term in $|\cdots|^2$ in Eq. (2)]:[22]

$$\begin{aligned}&\langle f_{\boldsymbol{p}}^-|v_m g(\varepsilon_p+\omega_m)\Delta|\phi_c\rangle\approx\tau_m^{\rm ex}(\boldsymbol{p})\langle f_{\boldsymbol{p}}^-|\Delta|\phi_c\rangle,\\&\tau_m^{\rm ex}(\boldsymbol{p})=(2\pi)^{3/2}\int d\boldsymbol{r}f_{\boldsymbol{p}}^{-*}(\boldsymbol{r})v_m(\boldsymbol{r})g_0(\boldsymbol{r}-\boldsymbol{R}_A;p').\end{aligned} \tag{28}$$

B. Quantum Landau formula

The overall photoemission profile is now written as the exponential form with the aid of the approximations discussed in the previous subsection, which recovers the lowest sum (up to the single losses) $I(\boldsymbol{p})^0+I(\boldsymbol{p})^1$, and satisfies the normalization condition:

$$\begin{aligned}I(\boldsymbol{p};\omega)_c^\infty=&\,|\langle f_{\boldsymbol{p}}^-|\Delta|\phi_c\rangle|^2\int_{-\infty}^{\infty}dt\exp[i(\omega+E_0-E_0^*-\varepsilon_p)t]\\&\times\exp\left[\int_0^\infty d\varepsilon\frac{\alpha(\varepsilon)}{\varepsilon}(e^{-i\varepsilon t}-1)\right].\end{aligned} \tag{29}$$

The function $\alpha(\epsilon)$ is a spectral function called "asymmetric function," which fully includes intrinsic and extrinsic losses defined by

$$\frac{\alpha(\epsilon)}{\epsilon}=\sum_m|\tau_m|^2\delta(\epsilon-\omega_m),\quad\tau_m(\boldsymbol{p})=\tau_m^{\rm ex}(\boldsymbol{p})+S_m/S_0. \tag{30}$$

This exponential form Eq. (29) is known as the Landau formula, which was derived on the basis of classical transport theory.[28] A very similar quantum derivation is developed by Hedin *et al.*[5,29] where time-reversed LEED function is used instead of the renormalized damping photoelectron wave function $f_{\boldsymbol{p}}^-$. Here the "time-reversed LEED function" is the damping plane wave only in the normal to the surface. It freely propagates without damping parallel to the surface. The generalization to $f_{\boldsymbol{p}}^-$ as shown in Eq. (28) is crucial to discuss the photoelectron diffraction effect and quantum depth distribution function (DDF).[24]

Both $\tau_m^{\rm ex}$ and S_m/S_0 can be written in terms of the fluctuation potential v_m. An explicit form of τ_m is thus written from Eqs. (7) and (30):

$$\tau_m(\boldsymbol{p})=\int f_A(\boldsymbol{r})v_m(\boldsymbol{r})d\boldsymbol{r}, \tag{31}$$

$$f_A(\boldsymbol{r})=-\frac{|\phi_c(\boldsymbol{r})|^2}{\epsilon}+(2\pi)^{3/2}f_{\boldsymbol{p}}^{-*}(\boldsymbol{r})g_0(\boldsymbol{r}-\boldsymbol{R}_A;p'), \tag{32}$$

where $\epsilon=\omega+E_0-E_0^*-\varepsilon_p$ is the excitation energy measured from the core threshold. The first term of f_A describes the intrinsic losses, whereas the second one describes the extrinsic losses. Assuming that v_m is real, we obtain an alternative expression for $\alpha(\epsilon)/\epsilon$:

$$\begin{aligned}\frac{\alpha(\epsilon)}{\epsilon}&=\int d\boldsymbol{r}d\boldsymbol{r}'f_A^*(\boldsymbol{r}')f_A(\boldsymbol{r})\sum_m v_m(\boldsymbol{r}')v_m(\boldsymbol{r})\delta(\omega-\omega_m)\\&=-\frac{1}{\pi}\int d\boldsymbol{r}d\boldsymbol{r}'f_A^*(\boldsymbol{r}')f_A(\boldsymbol{r}){\rm Im}W(\boldsymbol{r},\boldsymbol{r}';\epsilon),\end{aligned} \tag{33}$$

where $W(\epsilon)$ is the screened Coulomb propagator.[5,14,16] The spectral features of the loss spectra are primarily determined by $\alpha(\epsilon)/\epsilon$, which can be divided into three parts: the intrinsic, the extrinsic, and the interference parts.

For practical calculations, we use further approximations for the core electron distribution and the photoelectron wave function in Eq. (32):

$$\begin{aligned}&|\phi_c(\boldsymbol{r})|^2\approx\delta(\boldsymbol{r}-\boldsymbol{R}_A),\\&f_{\boldsymbol{p}}^-\approx\phi_{\boldsymbol{p}}^0(\boldsymbol{r})=\frac{1}{(2\pi)^{3/2}}\exp(i\,\boldsymbol{p}_\parallel\cdot\boldsymbol{r}_\parallel)\exp(i\tilde{p}z).\end{aligned} \tag{34}$$

The second approximation in Eq. (34) neglects the elastic scatterings for the loss function $\alpha(\epsilon)$, but the elastic scatterings are still taken into account in the calculation of the amplitude $\langle f_{\boldsymbol{p}}^-|\Delta|\phi_c\rangle$. The z component of the damping wave momentum $\tilde{p}$ is complex to explain the decay in photoelectron propagation along the z direction inside the solid, whereas the parallel component $\boldsymbol{p}_\parallel$ is real. Explicit formulas for these three parts in $\alpha(\epsilon)/\epsilon$ can be obtained with the aid of the above approximations. The superfix "int" refers to the intrinsic loss, and so on:

$$\frac{\alpha^{\rm int}(\epsilon)}{\epsilon}=-\frac{1}{\pi}{\rm Im}\left\{\int d\boldsymbol{r}d\boldsymbol{r}'\left[f_A^{\rm int}(\boldsymbol{r}')\right]^*f_A^{\rm int}(\boldsymbol{r})W(\boldsymbol{r},\boldsymbol{r}';\epsilon)\right\}=-\frac{1}{\pi|\epsilon|^2}{\rm Im}W(z_A,z_A;\epsilon), \tag{35}$$

$$\begin{aligned}\frac{\alpha^{\rm ext}(\epsilon)}{\epsilon}&=-\frac{1}{\pi}{\rm Im}\left\{\int d\boldsymbol{r}d\boldsymbol{r}'\left[f_A^{\rm ext}(\boldsymbol{r}')\right]^*f_A^{\rm ext}(\boldsymbol{r})W(\boldsymbol{r},\boldsymbol{r}';\epsilon)\right\}\\&=-\frac{1}{\pi|\tilde{\kappa}|^2}{\rm Im}\left[\int_{-\infty}^{\infty}dzdz'e^{i\tilde{p}(z'-z_A)}e^{-i\tilde{p}^*(z-z_A)}e^{i\tilde{\kappa}|z-z_A|}e^{-i\tilde{\kappa}^*|z'-z_A|}W(z,z';\epsilon)\right],\end{aligned} \tag{36}$$

$$\begin{aligned}\frac{\alpha^{\mathrm{inf}}(\epsilon)}{\epsilon} &= -\frac{1}{\pi}\mathrm{Im}\left(\int_{-\infty}^{\infty} d\boldsymbol{r}d\boldsymbol{r}'\left\{\left[f_A^{\mathrm{int}}(\boldsymbol{r}')\right]^* f_A^{\mathrm{ext}}(\boldsymbol{r}) + \left[f_A^{\mathrm{ext}}(\boldsymbol{r}')\right]^* f_A^{\mathrm{int}}(\boldsymbol{r})\right\} W(\boldsymbol{r},\boldsymbol{r}';\epsilon)\right)\\ &= -\frac{1}{\pi}\mathrm{Im}\left[\frac{i}{\epsilon^*\tilde{\kappa}}\int_{-\infty}^{\infty} dz e^{-i\tilde{p}^*(z-z_A)} e^{i\tilde{\kappa}|z-z_A|} W(z,z_A;\epsilon) - \frac{i}{\epsilon\tilde{\kappa}^*}\int_{-\infty}^{\infty} dz' e^{i\tilde{p}(z'-z_A)} e^{-i\tilde{\kappa}^*|z'-z_A|} W(z_A,z';\epsilon)\right]. \end{aligned} \quad (37)$$

Bechstedt's screened Coulomb potential W is used to calculate $\alpha(\epsilon)/\epsilon$ in the present work:[30]

$$\begin{aligned} W(z,z';\epsilon) = \frac{2\pi}{Q}[&\theta(z)\theta(z')\{e^{-Q|z-z'|} + (1-t_1)e^{-Q(z+z')}\} + t_1\{\theta(z)\theta(-z')a(-z')e^{-Qz} + \theta(-z)\theta(z')a(-z)e^{-Qz'}\}\\ &+ \theta(-z)\theta(-z')\{a(|z-z'|) + a(-z-z') - t_1 a(-z)a(-z')\}], \end{aligned} \quad (38)$$

where $t_1 = 2/\{1 + a(0)\}$, and $a(z) \equiv a(Q,z,\omega)$ is related to the bulk dielectric function $\epsilon_0(q,\omega)$, which is approximated by use of a single-plasmon pole formula:

$$a(Q,z,\omega) = \frac{Q}{\pi}\int dq_z \frac{e^{iq_z z}}{|\boldsymbol{q}|^2\epsilon_0(|\boldsymbol{q}|,\omega)}, \quad Q = \sqrt{q_x^2 + q_y^2}. \quad (39)$$

The screened Coulomb potential W has information on both surface and bulk plasmons.

Now we discuss only the single-plasmon (first) loss peak. From Eq. (29), we obtain the explicit expression for the single-loss spectra in terms of $\alpha(\epsilon)$:

$$I^1(\boldsymbol{p},\omega) = 2\pi|\langle f_{\boldsymbol{p}}^-|\Delta|\phi_c\rangle|^2 \frac{\alpha(\epsilon)}{\epsilon}\exp\left[-\int_0^{\infty} d\omega \frac{\alpha(\omega)}{\omega}\right]. \quad (40)$$

The present quantum Landau formula provides us with the double plasmon loss features in the second order terms of power series expansion of the Landau formula (29) in terms of $\alpha(\epsilon)/\epsilon$.

III. RESULTS AND DISCUSSION

Here we mainly consider the cases when the photoelectron detection direction $\boldsymbol{p}$ and the x-ray polarization $\boldsymbol{e}$ are nearly parallel. As described above, the quantum Landau formula is derived within the high-energy approximation and is basically not adequate in low kinetic energy region. Ohori *et al.* have studied the applicability of this formula.[20] They have shown that the quantum Landau formula can be safely used even in the intermediate energy region (say, several hundred eV) except for the case where $\boldsymbol{p}$ and $\boldsymbol{e}$ are nearly normal. Computational cost of the multiple-scattering calculation can be a bottleneck in this study. The calculations of $(1-X)^{-1}$ require much time. The maximum orbital angular momentum $l_{\max}$ from each atomic site increases with p. Here we study only intermediate energy region, say, $\varepsilon_p = 100$–200 eV.

A. Al 2s photoemission

Here we investigate single plasmon losses associated with Al 2s photoemission. The parameters used in the present calculations are given in Table I.

First we study the depth dependence of the loss spectral function β:

$$\beta(\epsilon) \equiv \alpha(\epsilon)/\epsilon. \quad (41)$$

As demonstrated in Eq. (40) this function directly describes the plasmon loss features, whereas $|\langle f_{\boldsymbol{p}}^-|\Delta|\phi_c\rangle|^2$ describes the XPD effects on the loss spectra. Figure 2 shows the spectral function $\beta(\epsilon)$ calculated for the photoemission from a (001) surface detected at polar angles of $\theta = 0^\circ$ (normal emission) and $\theta = 60^\circ$: The normal emission from various atomic layers are shown in the left column, and those for off-normal emission ($\theta = 60^\circ$) are shown in the right. For both cases peaks around 17 eV and 13 eV correspond to the bulk and the surface plasmon losses. The photon energy of the incident x-ray is fixed at 320 eV. The spectral function $\beta(\epsilon)$ describes only the loss processes which should not be influenced by the x-ray polarization. The depth dependence of the photoelectron emitters z_A is important for $\beta(\epsilon)$ as can be seen from Eqs. (35)–(38). "Total" means "(intrinsic) + (extrinsic) + (interference)." We should note that the intrinsic loss factor $\beta^{\mathrm{int}}(\epsilon)$ does not depend on the photoemission direction as can be seen from Eq. (35): the intrinsic loss factor $\beta^{\mathrm{int}}(\varepsilon)$ is the same for the two detection modes at the same $|z_A|$. In contrast the complex momenta inside the solids $\tilde{p}$ and $\tilde{\kappa}$ depend on the photoelectron momentum $\mathbf{p}$, and thus the extrinsic and the interference terms $\beta^{\mathrm{ext}}(\epsilon)$ and $\beta^{\mathrm{int}}(\varepsilon)$ are dependent on the detection angle. The loss profiles of $\beta(\epsilon)$ for the near surface layer ($z_A = -1.43$ Å) show only peaks due to surface plasmon excitation. For the deeper emitters, the peak intensity corresponding to bulk plasmon excitation gets stronger. We also observe the more prominent contribution from the extrinsic processes than that from the intrinsic losses. In the off-normal emission ($\theta = 60^\circ$) the extrinsic loss intensity grows much faster than the normal emission with z_A. The total loss intensities $\beta(\epsilon)$ in the off-normal emission from

TABLE I. Parameters for Al metal

Binding energy of 2s level	118 eV
Lattice structure	fcc
Lattice constant	4.05 Å
Plasmon energy	15.8 eV
Density parameter (r_s)	2.07
Work function	4.20 eV

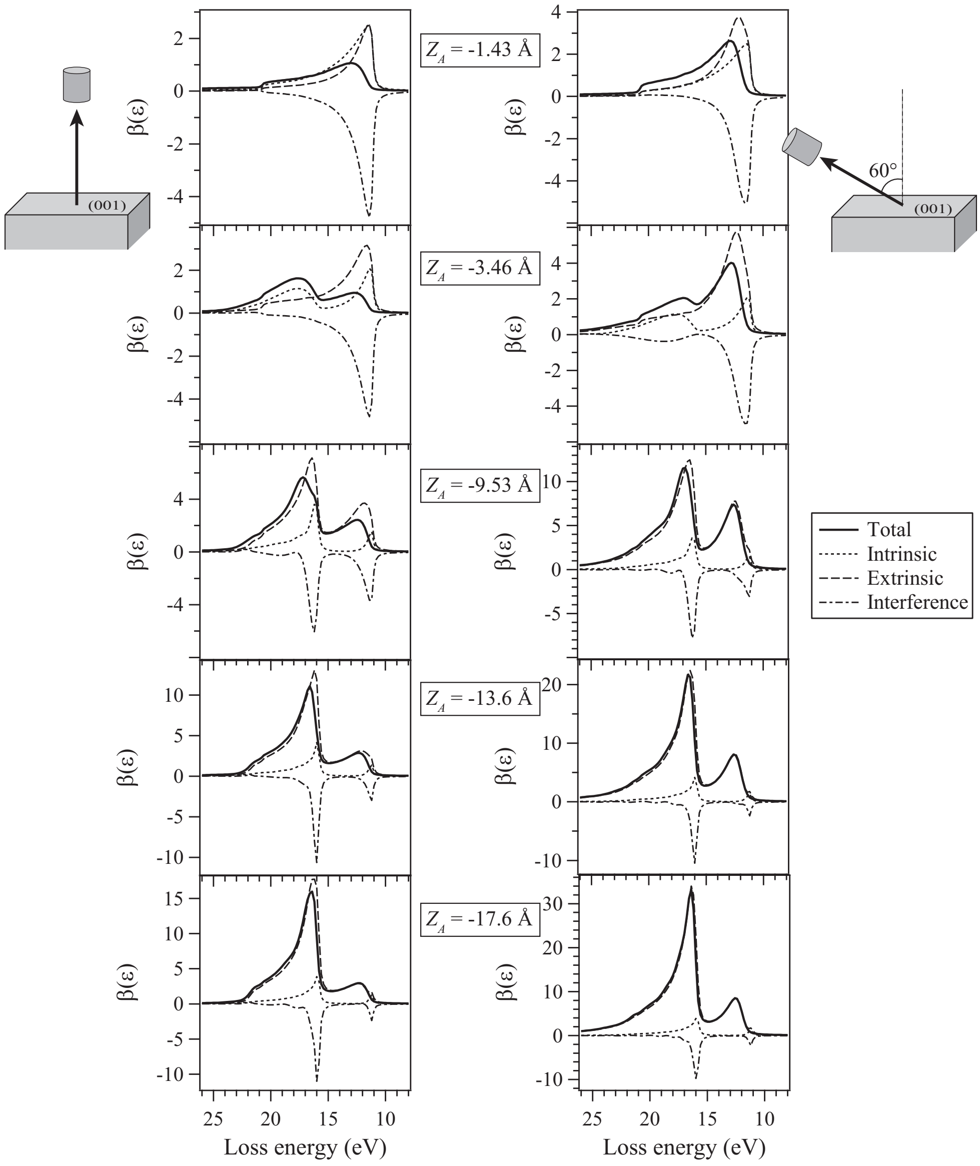

FIG. 2. Calculated loss spectral function $\beta(\epsilon)$ for plasmon losses associated with Al 2*s* photoemission detected in the different directions with polar angles of $\theta = 0^\circ$ and 60°. Photon energy is fixed at 320 eV. The depth of the photoelectron emitter $|z_A|$ is changed from 1.43 Å to 17.6 Å.

the deep emitters are thus stronger than those in the normal emission, which results in faster decay of the contribution from deeper sites due to the exponential part of Eq. (40). This effect also enhances the surface sensitivity of the plasmon losses in the off-normal emission, in addition to the long propagation distance from the emitters to the surface in the factor $| < f_{\mathbf{p}}^{-}|\Delta|\phi_c > |^2$.

Next we study depth profiles of the single-plasmon loss spectra. An incident x-ray is linearly polarized with tilt angle 10° away from the surface normal, and the photon energy is fixed at 320 eV: The schematic view of the setup is shown in Fig. 3. We have calculated the loss spectra using Eq. (40). The integrated surface + bulk plasmon loss intensities are shown for various depths of the photoelectron emitter z_A, which are shown in Fig. 4 as a function of z_A. We have used three types of approximations for the photoemission intensity $|\langle f_{\boldsymbol{p}}^{-}|\Delta|\phi_c\rangle|^2$ to study the elastic scattering effects (a) without elastic scattering [see Eq. (22)], (b) with single scatterings [see Eq. (24)], and (c) with full multiple scatterings [see Eq. (25)]. An aluminum cylinder

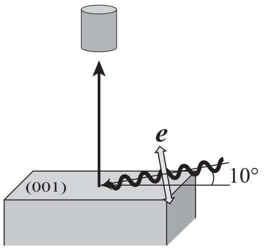

FIG. 3. The schematic view of the calculation setup. Incident x-ray is linearly polarized, whose electric vector tilts 10° from the surface normal.

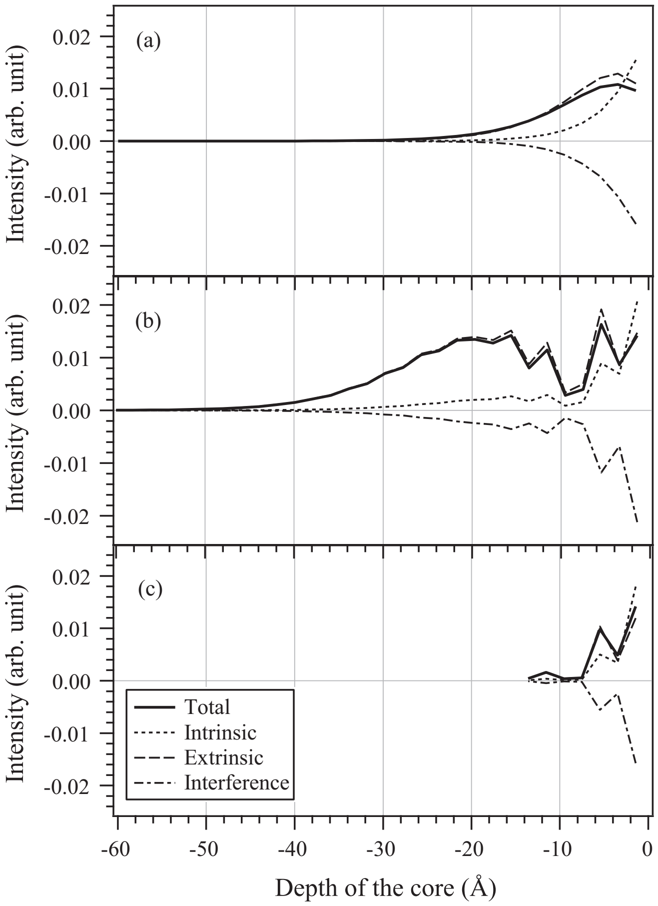

FIG. 4. Depth profiles of integrated surface and bulk single plasmon losses excited from the Al 2s level. The results are shown for those calculated without elastic scattering (a), with single scatterings (b), and with full multiple scatterings (c). The incident photon energy is 320 eV. The geometrical setup is shown in Fig. 3, and the cluster used here is shown in Fig. 5.

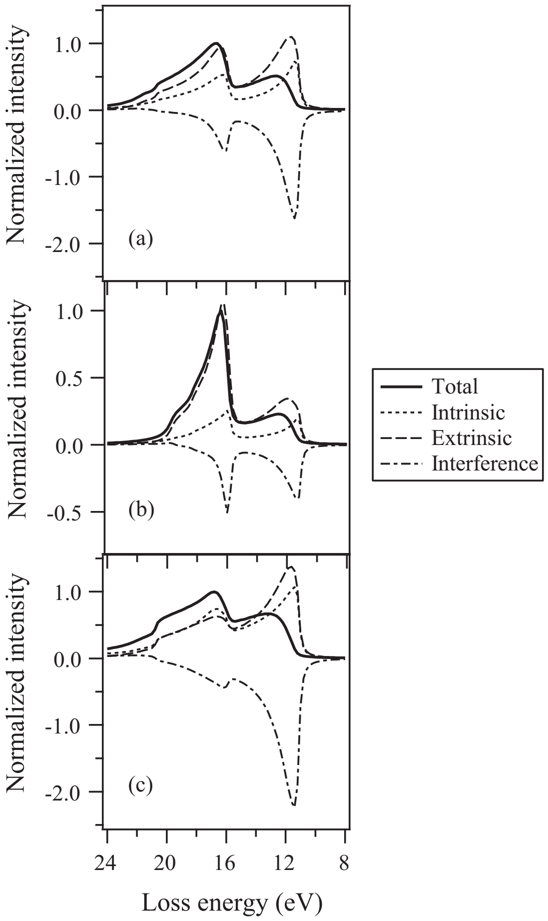

FIG. 6. Bulk and surface plasmon losses excited from Al 2s detected at normal emission calculated without elastic scattering (a), with single scatterings (b), and with full multiple scatterings (c). The incident photon energy is 320 eV. The spectra are normalized so that the peak intensities of bulk plasmon peaks are unity.

model including 48 atoms (seven layers, see Fig. 5) is used for the calculations. In the single-scattering approximation, the contribution of the photoemission from deep atomic sites is emphasized because of the *forward focusing effect*: The ejected electrons are strongly scattered from nearby atoms in the forward direction. The full multiple scatterings cause rapid decay with $|z_A|$ as shown in Fig. 4(c) in comparison with the result in Figs. 4(a) and 4(b). This behavior can be explained by the *defocusing effect*: It has been suggested on the basis of multiple-scattering calculations that if several atoms are linearly arranged along the emission direction, the destructive interference actually reduces the intensity.[31,32] This reduction is called the defocusing effect and has also been observed in experimental spectra.[33] Shinotsuka *et al.* have extensively studied the depth distribution function (DDF) using quantum mechanical multiple-scattering calculations and have demonstrated that the inclusion of full multiple scattering is necessary for the proper evaluation of DDF.[24] The oscillations in the loss intensity observed in Fig. 4(b) and 4(c) can be due to the photoelectron diffraction effects.[34]

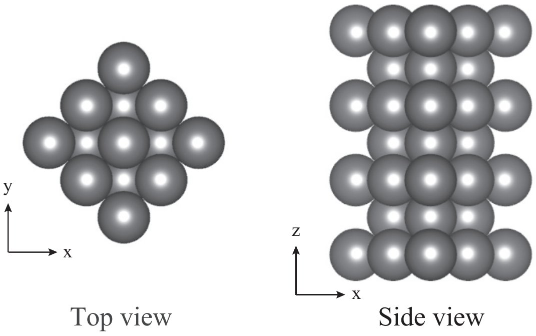

FIG. 5. Aluminum (001) cylinder model with seven layers having 48 atoms.

The Al 2s single-plasmon loss spectra, which can be compared with experimental loss spectra, are obtained by summing up the loss spectra from all the emitters shown in Fig. 4. Single-plasmon loss spectra calculated without elastic scattering, with single scatterings, and with full multiple scatterings are shown in Figs. 6(a), 6(b), and 6(c), respectively. The three spectra have been normalized so that the peak intensities of bulk plasmon peaks are to be unity. The single

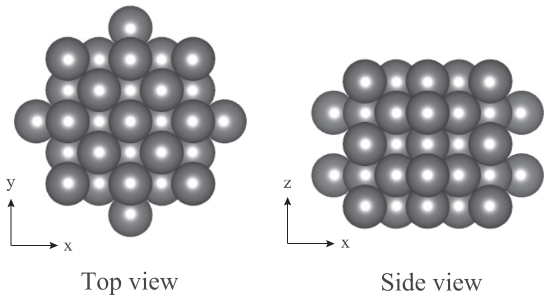

FIG. 7. Aluminum (001) cylinder model with five layers having 71 atoms used for the calculations in Figs. 8–13.

scattering approximation shown in Fig. 6(b) gives rise to a strong bulk plasmon loss peak, because the forward focusing effect enhances the photoemission from deep emitters as observed in Fig. 4(b). In contrast as demonstrated in Fig. 6(c) the surface plasmon losses are enhanced in comparison with the result in Fig. 6(b), because the plasmon loss intensity rapidly decays with $|z_A|$ as shown in Fig. 4(c). The plasmon loss spectra from deep emitters give quite strong bulk plasmon loss peaks as shown in Fig. 2 (see the left column for the normal emission). The deeper emitters than 10 Å have only a small contribution to the loss spectra, and the loss spectra in Figs. 6(a) and 6(c) are thus quite similar.

We have also calculated the loss spectra for the incident x-rays with the lower photon energy 220 eV. The detection mode is the same as that for the case with $\omega = 320$ eV (see Fig. 3). In this case we have used an Al cylinder model with five layers shown in Fig. 7: The model size along z direction is shorter than that used for the previous calculations at $\omega = 320$ eV because the electron mean free path becomes shorter. The mean free path is 7.4 Å for $\varepsilon_p = 202$ eV, whereas 5.1 Å for $\varepsilon_p = 102$ eV, values obtained by use of Hedin-Lundqvist potential. On the other hand, the size along the xy direction is increased; however, because the forward focusing effect becomes weaker for the lower energy, photoelectrons are more likely to be scattered with large scattering angle. The depth profiles of single-plasmon loss spectra without elastic scattering and with full multiple scatterings are shown in Figs. 8(a) and 8(b), and the single-plasmon loss spectra summed over all possible z_A are given in Figs. 9(a) and 9(b). Comparing those depth profiles with those excited by higher energy photons (320 eV) shown in Fig. 4, we find rapid decay with $|z_A|$ for the lower energy (220 eV) because of the shorter mean free path for the latter. Without elastic scatterings the depth dependence is similar to each other: They show structureless smooth decay with $|z_A|$. The full multiple scatterings have a strong influence on the depth profiles in Fig. 8(b), whereas the summed plasmon loss spectra shown in Fig. 9(b) are not influenced by the multiple scatterings so much. The pronounced structures in Fig. 8(b) are due to the photoelectron diffraction effects.

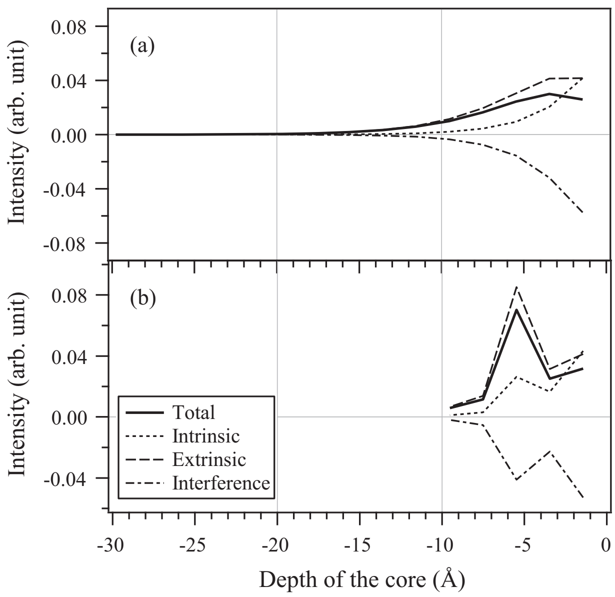

FIG. 8. Depth profiles of integrated surface and bulk single plasmon losses excited from Al 2*s* level for the incident photon energy 220 eV for the model shown in Fig. 3. The results are shown for those calculated without elastic scattering (a) and with full multiple scatterings (b).

Now we study the azimuthal intensity scan of the single plasmon loss peak of photoelectrons excited from Al 2*s* by x-rays with the photon energy 220 eV. Osterwalder *et al.* studied the azimuthal scan of Al 2*s* no-loss and loss peaks using Mg $K\alpha$ radiation, and they found that the loss peaks clearly reflect the local symmetry around an x-ray-absorbing atom just like the 2*s* main peak.[21] So far no one has succeeded in explaining that interesting angular behavior because elastic scatterings inside the solid have been completely neglected in Hedin's theory.[5] There the photoelectron state is described by the *time-reversed LEED function* $|\tilde{\boldsymbol{p}}\rangle$, which does not mean the full time-reversed LEED function including

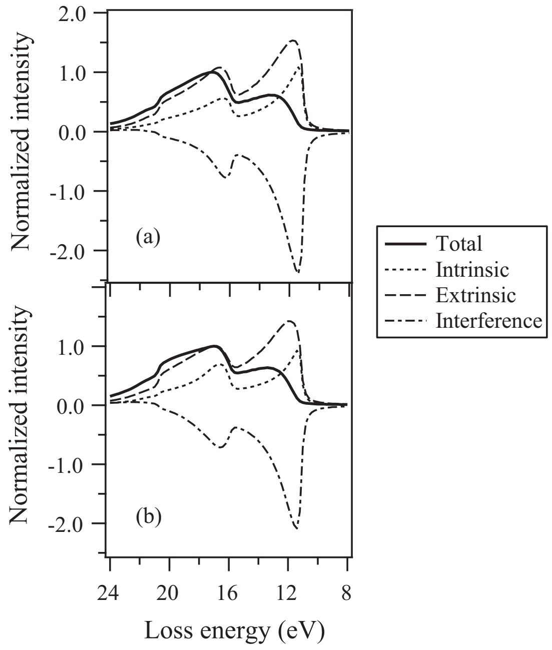

FIG. 9. Aluminum 2*s* plasmon losses at normal emission calculated without elastic scattering (a) and with full multiple scatterings (b). The incident photon energy is 220 eV. The spectra are normalized so that the peak intensity of the bulk plasmon peak is to be unity.

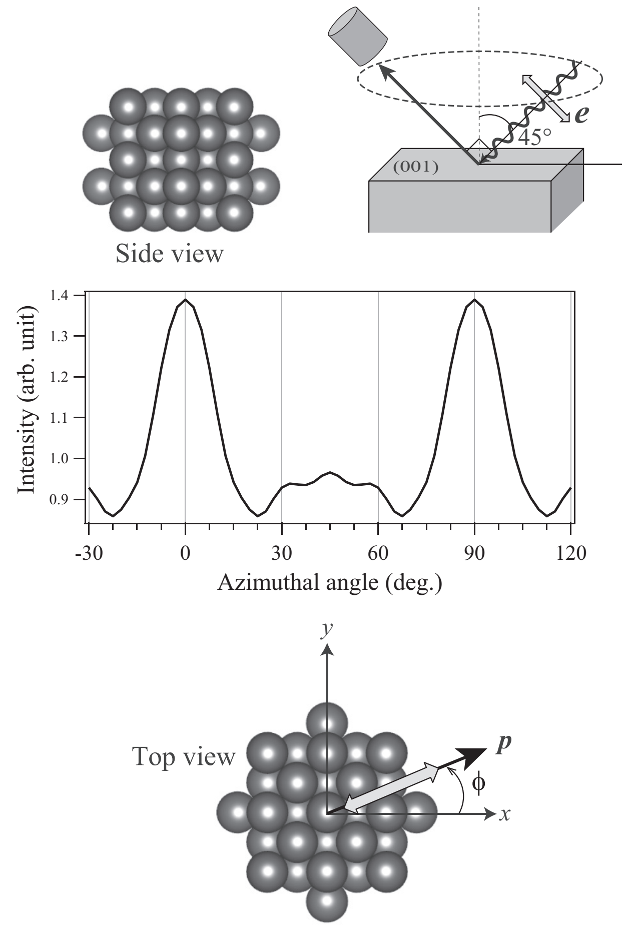

FIG. 10. Calculated azimuthal scan of the single bulk plasmon loss intensity associated with Al 2*s* core level from a (001) single crystal surface. The incident photon energy is 220 eV and loss energy is 15.8 eV; the polar detection angle is fixed at be $\theta = 45^\circ$. Full multiple scatterings are here taken into account.

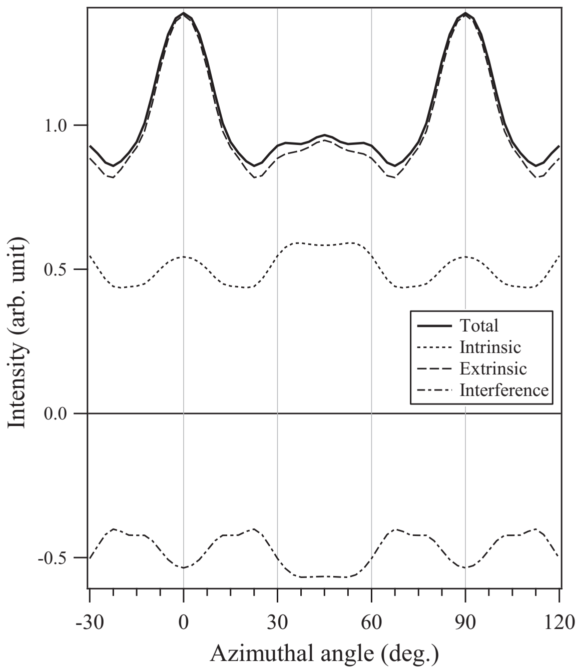

FIG. 11. Calculated azimuthal scans from a (001) for single plasmon loss associated with Al 2*s* core level from a Al single crystal surface model as shown in Fig. 10, but the total and three components, the intrinsic, extrinsic, and interference terms, are separately shown.

elastic scatterings from surrounding atoms in their paper; $\tilde{\boldsymbol{p}}$ is the same as the damping plane wave $\phi_{\boldsymbol{p}}^{0}$ shown in Eq. (34).

Figure 10 shows the calculated ϕ scan of the single bulk plasmon loss intensity from the Al(001) surface at a constant polar angle $\theta = 45^\circ$ with respect to the surface normal. Photon energy is fixed at 220 eV, and the linear polarization vector $\boldsymbol{e}$ is always set to be parallel to the photoelectron momentum $\boldsymbol{p}$. As the bulk plasmon loss energy is 15.8 eV, thus the photoelectron kinetic energy is 86 eV. Only the "total" spectrum is shown here. In the calculations of the loss intensity, the full-multiple scatterings are taken into account using the five-layer cylinder model. The calculated result clearly shows the fourfold symmetry. The strong peaks at 0° and 90° correspond to the directions to nearby atoms from the emitters. Figure 11 shows the ϕ scans of the three terms, the intrinsic, extrinsic, and interference terms, and the total loss (the sum of them). The intrinsic and the interference terms nearly cancel out each other, and the total loss is almost the same as the extrinsic term. As can be seen from the figure, the ϕ scan of the extrinsic loss is different from the intrinsic and the interference. The photoemission intensity $|\langle f_{\boldsymbol{p}}^{-}|\Delta|\phi_c\rangle|^2$ is common for all three terms, which is shown in Fig. 12. In the figure the XPD intensity ejected from each layer is shown. Of course, the XPD intensity from the first layer is dominant, which shows two prominent peaks at near 30° and 60°. In contrast, that from the second layer is much weaker in average than that from the first layer. We, however, observe the two sharp strong peaks at 0° and 90°. The XPD from the third layer also gives the three weak peaks at 0° and 90°, and also at 45°. These characteristic features are well explained from the atomic arrangement in the near surface region, and also the forward focusing scatterings. Summing up those ϕ scans from all layers, we obtain the total ϕ scan of the bulk plasmon loss, which gives rise to the two prominent peaks at 0°and 90°, and rather weak peaks near 30°, 45°, and 60°. In Fig. 2 the losses from deeper layers are enhanced, whereas the elastic scatterings from surrounding

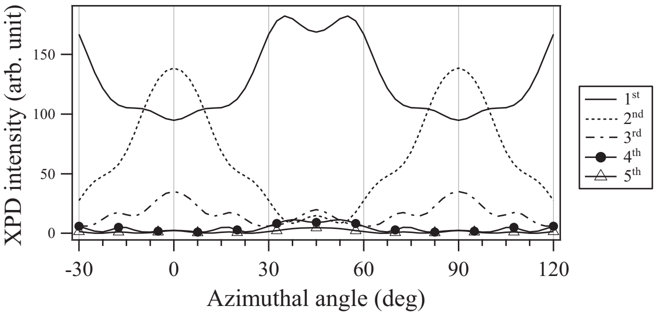

FIG. 12. The azimuthal scans of the loss spectra used in Figs. 10 and 11 are separately shown for each layer in Fig. 12. Full multiple scatterings are taken into account.

TABLE II. Parameters for Na metal

Binding energy of 2*s* level	63.3 eV
Lattice structure	bcc
Lattice constant	4.23 Å
Plasmon energy	5.9 eV
Density parameter (r_s)	3.92
Work function	2.36 eV

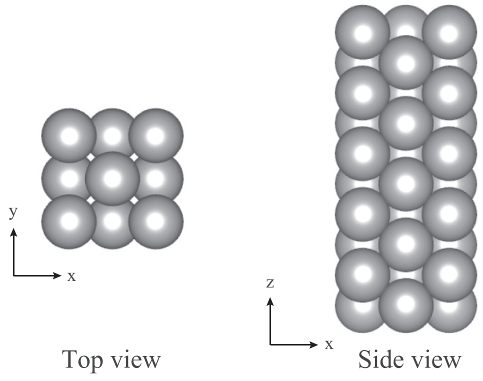

FIG. 14. Sodium (001) cylinder model including 45 atoms.

atoms are enhanced from shallow layers as usually observed in XPD spectra, in particular as expected for near normal emission.

Note that in the present calculations $\beta(\epsilon)$ does not show ϕ dependence, because now we replace the photoelectron wave function $f_{\boldsymbol{p}}^{-}$ in f_A [see Eq. (32)] by the damping plane wave $\phi_{\boldsymbol{p}}^{0}$, which completely neglects the elastic scatterings from surrounding atoms. If we calculate $f_{\boldsymbol{p}}^{-}$ taking elastic scatterings, the extrinsic part of f_A is dependent on the azimuthal angle ϕ and thus β^{ext} and β^{inf} depend on ϕ, though β^{int} is still constant. Then not only the photoelectron diffraction part $|\langle f_{\boldsymbol{p}}^{-}|\Delta|\phi_c\rangle|^2$ but also the spectral function $\beta(\epsilon)$ reflects the geometrical structure of the sample.

B. Na 2*s* photoemission

Here we show calculated results for single plasmon losses associated with Na 2*s* photoemission. Incident x-ray photon energy is fixed at 200 eV, and the geometrical setup is the same as that in Fig. 3. The parameters used in the present calculations are given in Table II.

Figure 13 shows the depth profiles of the single-loss spectra calculated without elastic scattering (a) and with full multiple scatterings (b). Sodium cylinder model including 45 atoms (10 layers[see Fig. 14) is used for the calculation of elastic scatterings. The inclusion of elastic scatterings causes the quite different depth profile from that without elastic scattering: Photoemissions from the third to seventh layers are emphasized in the latter. Figure 15 shows sodium 2*s* single plasmon loss spectra obtained by summing up the contributions from emitters. The two plasmon loss spectra shown in Figs. 15(a) and 15(b) are normalized so that the peak intensities of the bulk plasmon peaks are unity. In the "total" spectrum with full multiple scatterings, the relative peak intensity of (surface plasmon)/(bulk plasmon) is slightly smaller than that without elastic scattering, and their spectral features are quite similar although the depth profiles are quite different. Comparing the depth profiles in Fig. 13 and the loss spectra in Fig. 15 with those corresponding results for Al metal, we find quite similar characteristic features.

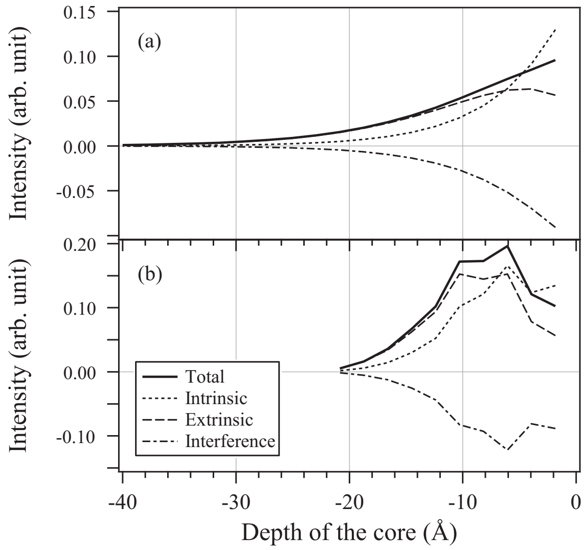

FIG. 13. Depth profiles of integrated single plasmon loss XPS intensities from Na 2*s* level calculated without elastic scattering (a) and with full multiple scatterings (b). The incident photon energy is 200 eV. The setup is shown in Fig 14.

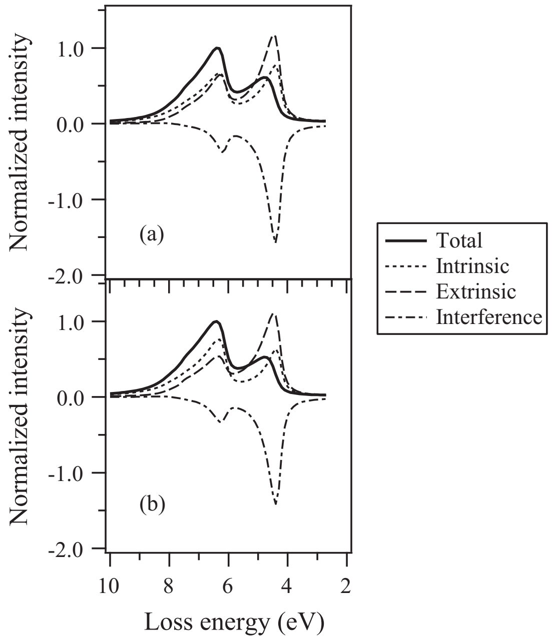

FIG. 15. Sodium 2*s* single plasmon loss spectra summed over all possible z_A calculated without elastic scattering (a) and with full multiple scatterings (b). The incident photon energy is 200 eV, and the calculation setup is given in Fig. 14.

IV. CONCLUDING REMARKS

In this paper we have studied plasmon losses associated with core-level photoemissions. Overall spectral features of x-ray photoelectron spectra can be described by the quantum Landau formula. One of the great advantages is that the quantum Landau formula allows us to calculate the multiple plasmon loss features: The calculations of the convolution $\beta(\epsilon)$ like $\beta * \beta * \cdots$ are only necessary. Within the semiclassical approximation multiple loss features are discussed in detail in Ref. 27. Our approach allows us to calculate the loss features in purely quantum theory.

With the aid of the approximations given in Eq. (23), we have succeeded in calculating single-plasmon loss spectra taking elastic scatterings into account. We thus can study the photoelectron diffraction effects before and after the losses in the plasmon loss peaks. We also have found that the elastic scatterings can considerably change the relative intensities of bulk and surface plasmon peaks, their peak shapes, which depend on composite elements and on energy. One of the important factors, the loss function $\beta(\epsilon)$ describes the spectral features of the plasmon loss spectra, which depends on the depth of the emitter. The loss spectra from the near surface and that from the deep emitters ($|z_A| \geqslant 10$Å) are quite different from each other. On the other hand, the depth profiles are mainly determined by the XPD factor $|\langle f_{\mathbf{p}}^{-}|\Delta|\phi_c\rangle|^2$. In the single elastic scattering approximation, the deeper emitters have much influence because of the forward focusing effects, whereas only the shallow emitters have dominant effects on the loss spectra because of the defocusing effects as discussed by Shinotsuka *et al.*[24]

Computational studies on the azimuthal scan of the loss peak explain well the observed angular dependence similar to that for the main photoemission band on the basis of the XPD factor, although the loss function $\beta(\epsilon)$ has its own angular dependence.

There are still some problems that need to be solved, however. One of them is to include elastic scattering effects in the calculation of the spectral function $\beta(\epsilon)$. So far we have calculated the spectral function using the damping plane wave instead of the full photoelectron wave function. Scattering effects can be basically included in the spectral function by the site T-matrix expansion of the photoelectron wave function just like we see in Sec. II.

Another major problem to overcome is rather technical: computational cost. For the multiple scattering calculations, we have to calculate the renormalized multiple scattering matrix $(1 - X)^{-1}$, which depends on ε_p: For large ε_p, the dimension of the matrix is quite large. We should thus restrict this to up to the soft x-ray region. If the single elastic scattering approximation were good to describe the loss features, we could overcome the problem. The present results, however, demonstrate the importance of the full multiple scattering calculations.

In this paper we have focused on the cases when the photoelectron momentum and the x-ray polarization vector are nearly parallel, where the quantum Landau formula can be safely used even in the low-energy region.[20] To study the behaviors when the photoelectron momentum $\mathbf{p}$ is nearly normal to the polarization vector $\mathbf{e}$, we need to consider a more accurate theoretical formula without use of the quantum Landau formula.

ACKNOWLEDGMENTS

M. Kazama is grateful for the financial support of a Grant-in-Aid for a JSPS fellow.

---

[*] niki@chiba-u.jp

[1] J. E. Inglesfield, J. Phys. C **16**, 403 (1983).

[2] T. Fujikawa, J. Phys. Soc. Jpn. **55**, 3244 (1986).

[3] T. Fujikawa, in *Core-Level Spectroscopy in Condensed Systems* (Springer, Berlin, 1988), p. 213.

[4] W. Bardyszewski and L. Hedin, Phys. Scr. **32**, 439 (1985).

[5] L. Hedin, J. Michiels, and J. Inglesfield, Phys. Rev. B **58**, 15565 (1998).

[6] T. Uwatoko, H. Tanaka, K. Nakayama, S. Nagamatsu, K. Hatada, T. Konishi, T. Fujikawa, T. Kinoshita, A. Harasawa, and A. Kakizaki, J. Surf. Sci. Jpn. **22**, 497 (2001).

[7] C. Biswas, A. K. Shukla, S. Banik, V. K. Ahire, and S. R. Barman, Phys. Rev. B **67**, 165416 (2003).

[8] A. Cohen Simonsen, Y. Yubero, and S. Tougaard, Phys. Rev. B **56**, 1612 (1997).

[9] S. Tougaard, Surf. Sci. **464**, 233 (2000).

[10] F. Yubero and S. Tougaard, Phys. Rev. B **71**, 045414 (2005).

[11] W. S. M. Werner, L. Kövér, S. Egri, J. Tóth, and D. Varga, Surf. Sci. **585**, 85 (2005).

[12] C. Caroli, D. Lederer-Rozenblatt, B. Roulet, and D. Saint-James, Phys. Rev. B **8**, 4552 (1973).

[13] C.-O. Almbladh, Phys. Scr. **32**, 341 (1985).

[14] T. Fujikawa and H. Arai, J. Elect. Spect. Relat. Phenom. **123**, 19 (2002).

[15] T. Fujikawa and H. Arai, Recent Res. Dev. Phys. **4**, 657 (2003).

[16] T. Fujikawa and H. Arai, Chem. Phys. Lett. **368**, 147 (2003).

[17] H. Arai and T. Fujikawa, Phys. Rev. B **72**, 075102 (2005).

[18] T. Fujikawa and H. Arai, J. Elect. Spect. Relat. Phenom. **149**, 61 (2005).

[19] T. Fujikawa, J. Elect. Spect. Relat. Phenom. **136**, 85 (2004).

[20] Y. Ohori, H. Shinotsuka, M. Kazama, and T. Fujikawa, e-J. Surf. Sci. Nanotech. **10**, 145 (2012).

[21] J. Osterwalder, T. Greber, S. Hüfner, and L. Schlapbach, Phys. Rev. B **41**, 12495 (1990).

[22] T. Fujikawa, M. Kazama, and H. Shinotsuka, e-J. Surf. Sci. Nanotech. **6**, 263 (2008).

[23] M. Kazama, H. Shinotsuka, Y. Ohori, and T. Fujikawa, e-J. Surf. Sci. Nanotech. **10**, 331 (2012).

[24] H. Shinotsuka, H. Arai, and T. Fujikawa, Phys. Rev. B **77**, 085404 (2008).

[25] J. M. de Leon, J. J. Rehr, C. R. Natoli, C. S. Fadley, and J. Osterwalder, Phys. Rev. B **39**, 5632 (1989).

[26] A. Chasse, J. Phys. Condens. Matt. **11**, 6475 (1999).

[27] P. Rennert, J. Electron Spectrosc. Relat. Phenom. **119**, 1 (2001).

[28] C.-O. Almbladh and L. Hedin, in *Handbook on Synchrotron Radiation*, edited by E. E. Koch (North-Holland, Amsterdam, 1983), Vol. 1b, p. 607.

[29] L. Hedin, in *Solid-State Photoemission and Related Methods*, edited by W. Schattke and M. A. Van Hove (Wiley-VCH, New York, 2003), Chap. 3, pp. 116–140.

[30] F. Bechstedt, R. Enderlein, and D. Reichardt, Phys. Status. Solidi B **117**, 261 (1983).

[31] S. Y. Tong, H. C. Poon, and D. R. Snider, Phys. Rev. B **32**, 2096 (1985).

[32] M.-L. Xu, J. J. Barton, and M. A. Van Hove, Phys. Rev. B **39**, 8275 (1989).

[33] S. Valeri, A. di Bona, and F. Borgatti, Surf. Sci. **371**, 143 (1997).

[34] M. Kazama, J. Adachi, H. Shinotsuka, M. Yamazaki, Y. Ohori, A. Yagishita, and T. Fujikawa, Chem. Phys. **373**, 261 (2010).